Global velocity field and bubbles in the blue compact dwarf galaxy Mrk 86

A. Gil de Paz,[★] J. Zamorano and J. Gallego

Dept. de Astrofísica, Universidad Complutense de Madrid, 28040 Madrid, Spain

ABSTRACT

We have studied the velocity field of the blue compact dwarf galaxy Mrk 86 (NGC 2537) using data provided by 14 long-slit optical spectra obtained in 10 different orientations and positions. This kinematical information is complemented with narrow-band ([O III]5007 Å and Hα) and broad-band (*B*, *V*, Gunn *r* and *K*) imaging. The analysis of the galaxy global velocity field suggests that the ionized gas could be distributed in a rotating inclined disc, with projected central angular velocity of $\Omega = 34\,\mathrm{km\,s^{-1}\,kpc^{-1}}$. The comparison between the stellar, H I and modelled dark matter density profile indicates that the total mass within its optical radius is dominated by the stellar component. Peculiarities observed in its velocity field can be explained by irregularities in the ionized gas distribution or local motions induced by star formation.

Kinematical evidences for two expanding bubbles, Mrk 86–B and Mrk 86–C, are given. They show expanding velocities of 34 and $17\,\mathrm{km\,s^{-1}}$, Hα luminosities of 3×10^{38} and $1.7 \times 10^{39}\,\mathrm{erg\,s^{-1}}$, and physical radii of 374 and 120 pc, respectively. The change in the [S II]/Hα, [N II]/Hα, [O II]/[O III] and [O III]/Hβ line ratios with the distance to the bubble precursor suggests a diminution in the ionization parameter and, in the case of Mrk 86–B, an enhancement of the shock-excited gas emission. The optical–near-infrared colours of the bubble precursors are characteristic of low-metallicity star-forming regions ($\sim 0.2\,\mathrm{Z_\odot}$) with burst strengths of about 1 per cent in mass.

Key words: ISM: bubbles – galaxies: compact – galaxies: individual: Mrk 86 – galaxies: irregular – galaxies: kinematics and dynamics.

1 INTRODUCTION

The study of the global velocity field of blue compact dwarf (BCD) galaxies (Thuan & Martin 1981) provides important clues about their gravitational potential, since these systems are rotationally supported (e.g. Van Zee, Skillman & Salzer 1998).

High spatial resolution H I observations have shown that the rotation curves of BCD galaxies (Meurer et al. 1998; Van Zee, Skillman & Salzer 1998) and dwarf irregulars (dI) (Moore 1994; Flores & Primack 1994) are nearly flat in the galaxy outer regions and have nearly constant velocity gradients within their optical radius. Also, optical studies of the velocity field of the ionized gas in BCDs obtain constant velocity gradients, characteristic of a solid-body rotation law (see Petrosian et al. 1997 for I Zw 18).

Although the neutral (see van Zee et al. 1998 and references therein) and molecular hydrogen (Young & Knezek 1989; Israel, Tacconi & Baas 1995) are quite abundant in BCDs and dIs, they are not enough to reproduce the flattening of the rotation curve. As in spiral galaxies, the existence of this flattening in the rotation curve of dwarf galaxies has been related with the presence of large

amounts of dark matter in galaxy outer regions (Carignan & Freeman 1988; Carignan & Beaulieu 1989; Broeils 1992). The dark matter content derived indicates that dark matter is even more abundant in dwarfs that in more massive galaxies (see Moore 1994 and references therein). In fact, standard cold dark matter (CDM) models predict that low-mass haloes are denser than more massive systems, because of their higher formation redshift (Navarro, Frenk & White 1997, hereafter NFW). The density profiles of the simulated CDM haloes fall with radius as r^{-2}. This is the density profile expected for a flat rotation-curve body.

The competition between the dark matter and the stellar mass components within the optical radius makes more difficult the analysis of the solid-body portion of the rotation curve. Several works have argued that dark matter in dwarf galaxies dominates the total mass density profile even within their optical radius (Carignan & Beaulieu 1989; Broeils 1992), showing a constant density dark matter core (Moore 1994; Flores & Primack 1994; Salucci & Persic 1997). On the other hand, Lo, Sargent & Young (1993) and Staveley-Smith, Davies & Kinman (1992) deduced reasonable virial mass to blue light ratios, $M_V/L_B < 7\,\mathrm{M_\odot/L_\odot}$, for a large fraction of their samples. Loose & Thuan (1986) found that the virial mass of Haro 2 can be reproduced just by adding the

★ E-mail: gil@astrax.fis.ucm.es

stellar and H I mass components. Also, the study by Swaters (1998) of the rotation curves of 44 dwarf galaxies indicates that the mass of a large fraction of these galaxies could be dominated by the stellar component, even at distances larger than three disc scalelengths.

One of the main sources of uncertainty in all these studies is the mass-to-light ratio adopted for the stellar component (Meurer et al. 1998; Swaters 1998). Therefore, high-quality optical and near-infrared imaging and spectroscopy are necessary in order to obtain the physical parameters of the stellar populations and derive reasonable mass-to-light ratios, thus preventing this uncertainty (which is inherent in this kind of kinematical study).

Superimposed on the regular solid-body portion of the velocity field, peculiar motions of the ionized gas have been observed in many star-forming dwarf galaxies (Tomita et al. 1997; Petrosian et al. 1997). These peculiar motions have commonly been explained as infalling motions of H II regions (Saitō et al. 1992), multiple clouds merging (Skillman & Kennicutt 1993) and local peculiar gas motions induced by violent star formation events (Petrosian et al. 1997). Very high star formation rates associated with these intense star-forming events have been shown to be able to produce a cavity of shock-heated gas arising from the energy input provided by supernovae and stellar winds (Chevalier & Clegg 1985; Vader 1986, 1987). This hot gas will accelerate the ambient interstellar medium, resulting in a collective supernova-driven wind. In fact, several galactic supernova-driven wind phenomena have been found to be associated with violent star formation places in dwarf galaxies (Roy et al. 1991; Izotov et al. 1996; Martin 1996, 1998, hereafter M98). They have generally been detected as holes in the neutral hydrogen distribution (Puche et al. 1992; Brinks 1994), bubbles or shells in Hα emission (Marlowe et al. 1995, hereafter MHW) or by their hot gas X-ray emission (Bomans, Chu & Hopp 1997).

The existence of these phenomena could produce the loss of a significant fraction of the galactic interstellar medium. Depending on the final destination of the accelerated gas, these structures could produce no mass loss; *blow-out*, only affecting the galactic chemical evolution; or *blow-away* processes, with a significant loss of interstellar mass (De Young & Gallagher 1990; M98; MacLow & Ferrara 1998). Consequently, these supernova-driven galactic winds are accepted as being a key parameter in dwarf galaxy formation (Silk, Wyse & Shields 1987; Mori et al. 1997) and evolution (MHW; MacLow & Ferrara 1998).

BCD galaxies, with intense recent or ongoing star-forming activity, are systems where it is more feasible to study the interplay between star formation and the interstellar medium. However, although the majority of the BCD galaxies are iE type BCDs ($\simeq 70$ per cent; Thuan 1991), with star formation spreading over the whole galaxy, the effects of the supernova-driven winds have been mainly studied in dwarf amorphous galaxies (see, e.g., MHW), which show nuclear star-forming activity.

The galaxy Mrk 86 = NGC 2537 (Shapley & Ames 1932; Markarian 1969), also known as Arp 6 (Arp 1966), constitutes an excellent laboratory in which to test the properties and effects of the supernova-driven winds on the interstellar medium of dwarf galaxies, as a nearby prototype of the iE BCD galaxies class.

After introducing Mrk 86 in Section 2, we describe the observations and data reduction in Section 3. Results on the global velocity field of Mrk 86 are given in Section 4. In Section 5.1 we describe the evolutionary synthesis models applied. Then, we show the physical properties of the Mrk 86–A (M98) expanding

bubble (Section 5.2), and the new bubbles detected in Mrk 86–B and Mrk 86–C (Sections 5.3 and 5.4). The velocity dispersion measured in Mrk 86–C is also discussed in Section 6. Finally, our summary and conclusions are given in Section 7. We have used $H_0 = 50$ km s^{-1} Mpc^{-1} and $q_0 = 0.5$ through this paper.

2 MRK 86

The galaxy Mrk 86 [$\alpha(1950) = 08^{\rm h} 09^{\rm m} 43^{\rm s}$; $\delta(1950) = +46° 08' 33''$], as a prototype of the iE type BCD galaxies, is characterized by a smooth elliptical low-surface-brightness underlying stellar component on which several irregular knots of star formation are superimposed (see Fig. 1 for a *B*-band image). Up to 50 different knots have been detected (Gil de Paz et al. 1999, in preparation, hereafter G99). In Fig. 2 we show those line-emitting regions with Hα surface brightness higher than 1.5×10^{-16} erg s^{-1} cm^{-2}. Assuming a receding velocity of 443 km s^{-1} (de Vaucouleurs & Pence 1980), the distance to Mrk 86 would be 8.9 Mpc and the physical scale 42.9 pc arcsec^{-1}. Mrk 86 has an absolute magnitude of $M_B = -17$ mag, and it has been detected on 1.2, 2.8 and 6.3 cm (Klein, Wielebinski & Thuan 1984; Klein, Weiland & Brinks 1991); the galaxy is a source of H I 21-cm emission (Thuan & Martin 1981; Bottinelli et al. 1984; WHISP survey, Kamphuis, Sijbring & van Albada 1996); it has also been detected in CO (Verter 1985; Sage et al. 1992); it is a strong *IRAS* source (Lonsdale et al. 1985; Dultzin-Hacyan, Masegosa & Moles 1990); near-infrared data were obtained by Thuan (1983); optical images were obtained by Hodge & Kennicutt (1983), Loose & Thuan (1985) and Ojha & Joshi (1991); and, finally, ultraviolet spectra have been analysed by Fanelli, O'Conell & Thuan (1988) and Longo, Capaccioli & Ceriello (1991) .

Papaderos et al. (1996a,b; P96a and P96b hereafter) obtained the physical parameters of the plateau, *central* and *exponential* photometric components. These components have been related
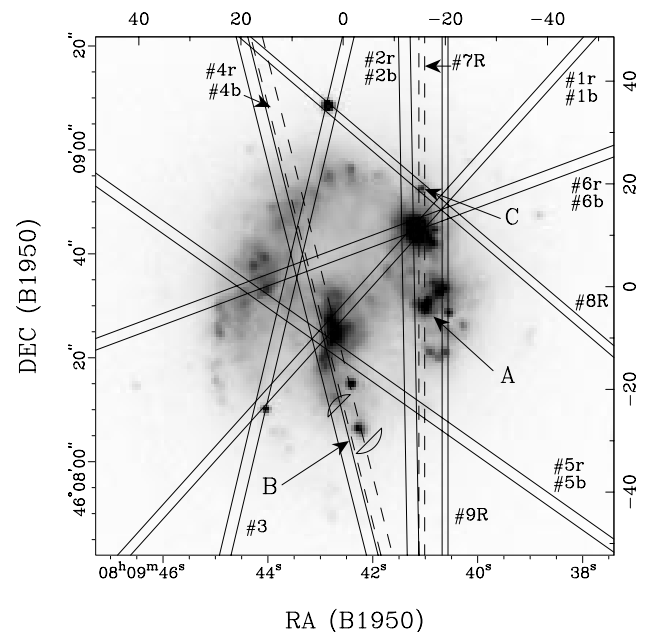

Figure 1. Long-slit positions superimposed on the Mrk 86 *B*-band image. Close to region B, size and position of the Mrk 86–B bubble Hα lobes are shown (see Figs 10a and 10b). Relative coordinates (in arcsec) are referred to the *r*-band outer isophotes centre.
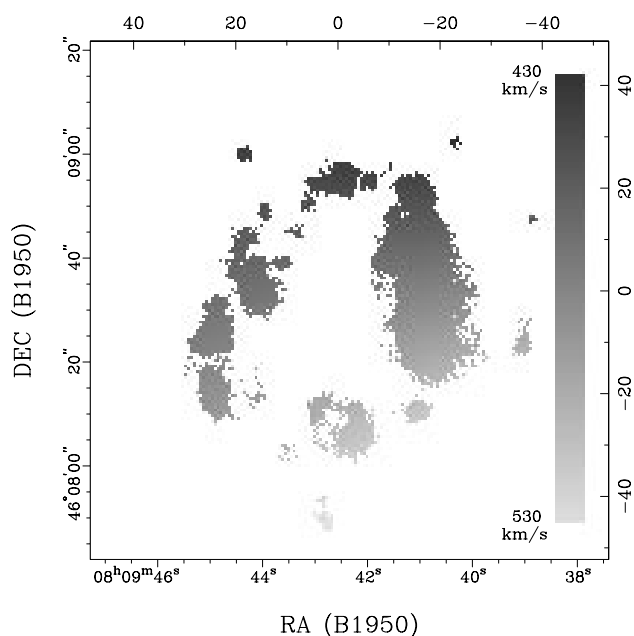
Figure 2. Interpolated 2D velocity field. Only regions with $\Sigma_{H\alpha} > 1.5 \times 10^{-16}\,\mathrm{erg\,s^{-1}\,cm^{-2}\,arcsec^{-2}}$ are shown.

Table 1. Journal of observations.

Telescope	Exp. time (s)	Slit	Spectral range (nm)	Disper. ($\mathrm{\AA\,pixel^{-1}}$)
		Spectroscopic observations		
CAHA 2.2-m	3600	1,2,4,6b	330–580	2.65
CAHA 2.2-m	1800	5b	330–580	2.65
CAHA 2.2-m	3600	1,2,4,5,6r	435–704	2.65
CAHA 2.2-m	3600	3	390–650	2.65
INT 2.5-m	1800	7,8R	637–677	0.39
INT 2.5-m	900	9R	637–677	0.39

Telescope	Exp time (s)	Filter	Scale (arcsec pixel^{-1})	PSF (arcsec)
		Image observations		
JKT 1.0-m	600	*B*	0.33	1.0
CAHA 1.5-m	2400	*V*	0.33	1.6
CAHA 2.2-m	600	Gunn-*r*	0.27	1.9
INT 2.5-m	900	Hα	0.57	2.3
INT 2.5-m	900	[O III]	0.57	2.5
UKIRT 3.8-m	100	*K*	0.60	1.4

with three different stellar populations (respectively: currently forming, $\simeq 1\,\mathrm{Gyr}$ and $\geq 7\,\mathrm{Gyr}$ old; Gil de Paz, Zamorano & Gallego 1998, hereafter G98).

3 OBSERVATIONS AND REDUCTIONS

We have obtained a total of 14 long-slit optical spectra in 10 different orientations and positions (see Fig. 1). The journal of spectroscopic observations is given in Table 1. Low- to intermediate-resolution spectra [full width at half-maximum (FWHM) = 6 Å in the light of Hα] with dispersion 2.65 Å pixel^{-1} were obtained with the Boller & Chivens spectrograph at the Cassegrain focus of the 2.2-m telescope at Calar Alto (Almería, Spain) in 1993 January. We used a 1024×1024 Tek 24-μm CCD. High-resolution spectra (FWHM = 0.9 Å in Hα and 0.39 Å pixel^{-1}; slits #7R, #8R and #9R) were obtained using the IDS instrument at

the Isaac Newton Telescope (INT) of the Observatorio del Roque de los Muchachos (La Palma, Spain) in 1998 January. The detector was a 1024×1024 Tek 24-μm CCD. The spectra were reduced, wavelength and flux calibrated, using standard FIGARO (1993 January) and IRAF procedures (1998 January), and making use of the corresponding standard stars and lamp calibration spectra. Line fluxes were measured using the IRAF task SPLOT, obtaining errors lower than 15 per cent.

We have also obtained *B*-, *V*-, *r*- and *K*-band images in different observing runs as described in Table 1. A Gunn *r*-band image was obtained at the 2.2-m telescope at Calar Alto in 1992 February with a GEC CCD with 30 μm 800×1156 pixel. The Johnson *V*-band image was obtained at the 1.52-m telescope at Calar Alto in 1993 December with a 19 μm 1024×1024 pixel CCD. A *B*-band image was obtained at the 1-m Jacobus Kapteyn Telescope (JKT) at the Observatorio del Roque de los Muchachos in 1997 November with a 24-μm 1024×1024 pixel Tek CCD. Finally, the near-infrared *K*-band image was obtained at the 3.8-m UKIRT telescope at Mauna Kea Observatory in 1993 April. We used the 62×58 InSb array camera IRCAM. Broad-band images were reduced using standard MIDAS and IRAF procedures. The procedures described by Aragón-Salamanca et al. (1993) were employed for the reduction of the K-band near-infrared image. All the broad-band images were calibrated observing standard stars at different airmasses.

Additional narrow-band images were secured for us during service time at the 2.5-m Isaac Newton Telescope at the Observatorio del Roque de los Muchachos in 1993 December. The detector was an EEV CCD with 1280×1180 22.5-μm pixel. [O III]5007 Å ($\lambda_0 = 5014$ Å; FWHM = 50 Å) and on/off Hα ($\lambda_0^{\mathrm{on}} = 6556$ Å, FWHM = 60 Å; $\lambda_0^{\mathrm{off}} = 6607$ Å, FWHM = 53 Å) images were obtained. The continuum subtraction was performed using, respectively for [O III] and Hα, the *V*-band and off-Hα images.

The [O III] and Hα images were flux calibrated as follows. First we convolved the *b* (blue-arm; see Table 1) spectra with the [O III] filter and the *r* (red-arm) spectra with the Hα filter (see Table 1 and Fig. 1). Then we collapsed these spectra in wavelength, obtaining the flux-calibrated spatial profile of the [O III] and Hα emission. We then cropped and averaged in the [O III] and Hα images those regions covered by the *b* and *r* slits, obtaining the [O III] and Hα spatial profiles given by the images. Comparing these spatial profiles with those obtained from the spectra, we calibrated both the [O III] and Hα images. Finally, these calibration relations were corrected for the sensitivity of the filters at the corresponding wavelength and, in the case of the Hα emission, from the contribution of the [N II]6548- and 6583-Å lines. The reliability of this method was demonstrated after applying it to all the blue-arm and red-arm spectra, and obtaining similar results within an error of 10 per cent.

4 GLOBAL VELOCITY FIELD

We have obtained the spatial variation of the ionized gas velocities using the long-slit spectra. We have used the RVDLINES IRAF task measuring the [O II]3727 Å, Hβ, [O III]4959 Å and [O III]5007 Å line velocities for the blue-arm spectra, and [O III]4959 Å, [O III]5007 Å, [N II]6548 Å, Hα, [N II]6583 Å, [S II]6717 Å and [S II]6731 Å for the red-arm spectra, weighted with their relative intensities. No significant differences were observed using

allowed and forbidden lines separately. Errors in the velocity were estimated where several emission lines could be measured (see Fig. 3).

From the velocities determined in the spectra, and the slit positions given in Fig. 1, we have reconstructed a 2D velocity map (see Fig. 2) using the IRAF task XYZTOIM. A careful examination of the interpolated 2D velocity fields yield a global solid-body velocity field of maximum velocity gradient $\Omega = 34 \, \mathrm{km \, s^{-1} \, kpc^{-1}}$ and orientation PA $\simeq 12°$ (rotation axis PA $\simeq -78°$). The heliocentric velocity measured at the galactic centre, as given by the r-band outer isophotes centre, is about $470 \, \mathrm{km \, s^{-1}}$. Although De Vaucouleurs & Pence (1980) gave a median heliocentric velocity of $443 \, \mathrm{km \, s^{-1}}$, a detailed examination of their Fabry–Perot interferogram shows that the velocity close to the galactic centre is significantly higher, between 450 and $460 \, \mathrm{km \, s^{-1}}$.

In Fig. 3 we show the velocity profiles measured along slits #9R, #7R, #2b, #2r, #4b and #4r, those positioned closer to PA = 12°. The six panels have been arranged in slit position order, from west to east, where slit #4b is that which closely crosses the galactic centre, as defined by the r-band outer isophotes [$\alpha(1950) = 08^h 09^m 42\overset{s}{.}56$; $\delta(1950) = +46° 08' 33\overset{''}{.}8$]. The northernmost part of the slit is represented at the left-hand side of each panel.

The panels (a) and (b) (slits #9R and #7R) show two different

velocity components, one very steep gradient and a second flatter velocity gradient. The steeper components seem to be associated with regions of enhanced K-band luminosity and relatively high star-forming activity (EW$_{\mathrm{H}\alpha} \sim 100 \, \mathrm{\mathring{A}}$), i.e. the emission knots #15 [$\alpha(1950) = 08^h 09^m 41\overset{s}{.}17$; $\delta(1950) = +46° 08' 45\overset{''}{.}1$; G99] and #16 [$\alpha(1950) = 08^h 09^m 41\overset{s}{.}00$; $\delta(1950) = +46° 08' 43\overset{''}{.}0$; G99; see Fig. 3]. This increase in the radial velocity gradient could be the result of an enhancement of the mass density over the global mass density distribution, related to the presence of these massive star-forming regions. However, a merging with another dwarf galaxy or gas cloud with an independent velocity field, as has been proposed to explain the velocity field of I Zw 18 (Skillman & Kennicutt 1993) and II Zw 40 (van Zee, Skillman & Salzer 1998), should not be ruled out. In that case, this merging could be responsible for the triggering of the star formation in the emission knots #15 and #16 (G99).

On the other hand, the #9R and #7R flat components and the gradients measured along the slits #2b, #2r and #4r should be related to a more relaxed global velocity field. In Table 2 we give these velocity gradients, being ω_0 (the gradients measured along the slits) and ω [the values projected to PA = 12°, i.e. $\omega_0 = \omega \times \cos(\mathrm{PA} - 12°)$]. Velocities affected by local motions, such as supernova-driven winds (see Section 5, below) have not been included in the calculus of the velocity gradients. From Table 2 we
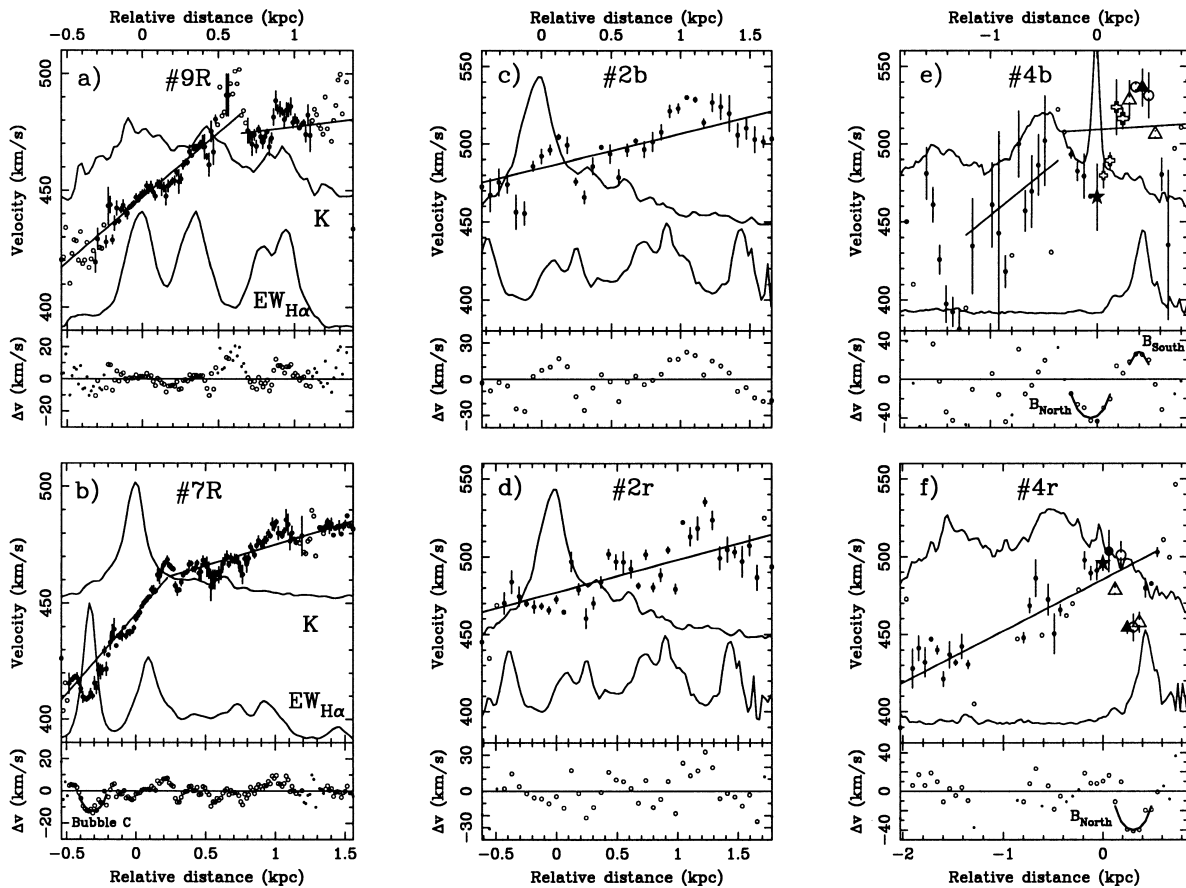

Figure 3. Heliocentric velocity profiles compared with the K-band and EW$_{\mathrm{H}\alpha}$ profiles: (a) Slit #9R. (b) Slit #7R. (c) Slit #2b. (d) Slit #2r. (e) Slit #4b. (f) Slit #4r. Special symbols used in panels (e) and (f) correspond to those regions marked in the left panel of the Fig. 10. Open circles are velocity data obtained from just one emission line, meanwhile filled circles are those measured using several emission lines. The peak in the EW$_{\mathrm{H}\alpha}$ profile of the panel (a) has been taken as reference for relative distances in this figure and it is due to the contribution from the close knot #16 (G99). The same for the panels (b), (c) and (d) and the knot #15 (see Fig. 9). Distances in the panels (e) and (f) are referred to the slit region closer to the field star position (see Fig. 10). Lower panels show the residuals from the global velocity gradient fitted.

Table 2. Velocity gradients. ω_0 are the velocity gradients measured along the slits, while ω are the values projected to PA = 12°. Distances along the rotation axis, d, have been measured relative to the r-band outer isophotes centre. The central value has been estimated from the interpolated 2D velocity map.

d (kpc)	ω_0 (km s^{-1} kpc^{-1}) Steep/flat comp.	ω (km s^{-1} kpc^{-1}) Steep/flat comp.	Slit
1.03	$55 \pm 4/8 \pm 3$	$56 \pm 5/8 \pm 3$	#9R
0.85	$69 \pm 5/18 \pm 2$	$70 \pm 5/19 \pm 2$	#7R
0.73	21 ± 4	21 ± 4	#2r
0.73	22 ± 5	22 ± 5	#2b
0.00		34 ± 5	
-0.12	33 ± 4	33 ± 4	#4r
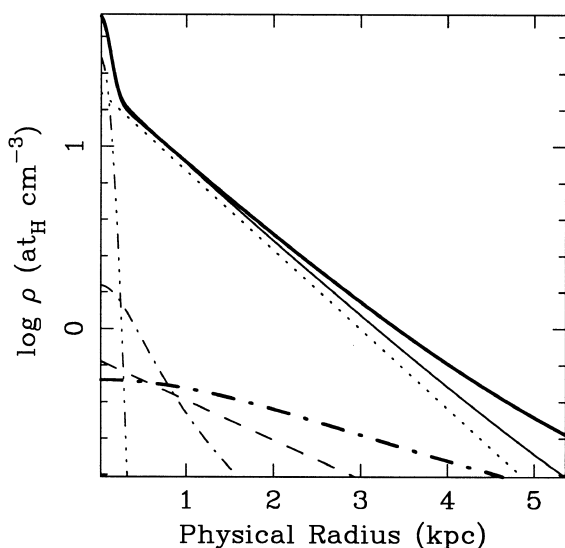
Figure 4. Thin lines: neutral hydrogen (dashed), stellar-underlying (dotted), stellar-starburst (dot-dot-dot-dashed), dark matter (dot-dashed) and total (solid) mass density profiles for $R_{\mathrm{DM}} = 0.5$ kpc. Thick lines: dark matter (dot-dashed) and total (solid) mass density profiles for $R_{\mathrm{DM}} = 3.0$ kpc.

see that the flat component of the velocity gradient grows from 10–20 km s^{-1} kpc^{-1} in the outer galaxy regions to ∼34 km s^{-1} kpc^{-1} close to the galactic centre.

4.1 Mass density profile

We will assume that the motion of the H II regions, which produce the observed line emission, is a result of rotation. Slit #4r was placed very close (∼3 arcsec) along the galactic equator. Therefore, we could compare its velocity profile with the radial component of the circular velocity curve (Binney, Tremain & Ostriker 1987). We will parametrize the mass distribution of the galaxy (stellar and dark matter, and neutral and molecular hydrogen). We have assumed that the photometric centre, given by the r-band outer isophotes, coincides with the kinematical centre (see Östlin et al. 1998). In order to compare the velocity curve, obtained along slit #4r with the radial component of the circular velocity curve, we will adopt the radial velocity measured close to the galactic centre as the systemic velocity.

Stellar. From the analysis of the surface brightness profiles of 14 BCD galaxies, P96a found that these profiles can be fitted

using three distinct components, the underlying, plateau and starburst components. Using a numerical deprojection procedure, they obtained the central luminosity densities and scale lengths for these components. G98 estimated the ages for the starburst and underlying components to be, respectively, 1 and 7 Gyr, with one-fifth solar metallicity. Then, we have taken the mass-to-light ratios predicted by the Bruzual & Charlot (private communication) evolutionary synthesis models for these ages and metallicities, under the assumption of instantaneous star formation and using an Scalo IMF (Scalo 1986). These mass-to-light ratios result in $M/L_B = 0.5 \, \mathrm{M_\odot/L_\odot}$ for the starburst component and $M/L_B = 2.6 \, \mathrm{M_\odot/L_\odot}$ for the underlying component. Although quite significant in luminosity, the plateau component represents a very small fraction in mass because its luminosity is produced by regions in which star formation is more recent than 20 Myr (G99), and that have mass-to-light ratios lower than $M/L_B = 0.08 \, \mathrm{M_\odot/L_\odot}$ (Bruzual & Charlot, private communication).

Finally, using the parameters given by P96a for the Mrk 86 starburst and underlying components, we obtain

$$\rho^{\mathrm{under}}(r) = \rho_0^{\mathrm{under}} \exp\left(-r/R_{\mathrm{under}}\right) \qquad (1)$$

$$\rho^{\mathrm{sb}}(r) = \rho_0^{\mathrm{sb}} \exp\left(-r/R_{\mathrm{sb}}\right)^2, \qquad (2)$$

where

$$\rho_0^{\mathrm{under}} = 20 \, \mathrm{at_H \, cm^{-3}},$$

$$R_{\mathrm{under}} = 1.0 \, \mathrm{kpc},$$

$$\rho_0^{\mathrm{sb}} = 31 \, \mathrm{at_H \, cm^{-3}},$$

$$R_{\mathrm{sb}} = 0.14 \, \mathrm{kpc}.$$

Neutral hydrogen. If we assume that the H I distribution, as given by the WHISP survey[1] falls approximately as an exponential function, and using the same deprojection procedure that for the optical data (see P96a), we obtain

$$\rho^{\mathrm{H\,I}}(r) = \rho_0^{\mathrm{H\,I}} \exp(-r/R_{\mathrm{H\,I}}) \qquad (3)$$

where

$$\rho_0^{\mathrm{H\,I}} \simeq 0.7 \, \mathrm{at_H \, cm^{-3}},$$

$$R_{\mathrm{H\,I}} \simeq 2.0 \, \mathrm{kpc}.$$

Molecular hydrogen. Sage et al. (1992) gave a M(H$_2$)/M(H I) ratio for Mrk 86 of 0.03. Therefore, we can assume that the effect of the molecular hydrogen in the gravitational potential of Mrk 86 is negligible.

Dark matter. Finally, we have considered the effect of the dark matter distribution over the global velocity field. Following the most recent observational works (Salucci & Persic 1997; Flores & Primack 1994; Moore 1994) and the study of Navarro, Eke & Frenk (1996) concerning the effects of supernova-driven winds over standard CDM profiles, we have assumed the existence of a central core in our dark matter density profile. Both the density distribution of a modified isothermal sphere (see Binney, Tremain & Ostriker 1987) and the universal profile given by Burkert (1995) include this central core and reproduce the observations reasonably. We have used, for this work, the simpler modified

---

[1] http://www.thales.astro.rug.nl/~whisp/Database/

isothermal profile, also following MacLow & Ferrara (1998),

$$\rho^{DM}(r) = \frac{\rho_0^{DM}}{1 + (r/R_{DM})^2}. \quad (4)$$

Burkert (1995; see also MacLow & Ferrara 1998) has shown that the central density ρ_0^{DM} is related to the scale radius R_{DM} through the expression

$$\rho_0^{DM} = 2.7 \times 10^7 \left(\frac{R_{DM}}{kpc}\right)^{-2/3} M_\odot \, kpc^{-3}. \quad (5)$$

Thus, this profile has only one free parameter, R_{DM}.

In Fig. 4 we show the total and DM mass density profiles for $R_{DM} = 0.5$ and 3 kpc. In both cases we see that the total mass density profile is dominated by the stellar component within the central 4 kpc.

Now, we could compare the radial component of the circular

Figure 5. Position angles, i and i_e, and coordinates x and y for two equatorial H II regions (#1 and #2). Solid plane represents the galactic equator.

velocity curve derived from the total density profile with the radial velocity data obtained along the slit #4r, placed close along the galactic equator. However, since the ionized gas emission is produced in several individual H II regions, the projected radial component of the modelled circular velocity will depend on the position of the corresponding H II region.

4.2 Ionized gas geometry

We will compare the velocity data obtained along the equatorial slit #4r with the projection of the rotation curve, adopting several geometries.

We will assume that the ionized gas is distributed in a thin disc with inclination i. This angle measures the inclination of its rotation axis with regard to the plane of the sky (i.e. $i = 0°$ for an edge-on disc; see Fig. 5). In the Fig. 5 we also show how the angles i and i_e and the coordinates x and y describe the position in the disc of an H II region. Under the hypothesis of 'thin disc', if $i \neq 0°$ only those regions with angle $i_e \simeq 0°$ will be observed through the slit #4r. This is the case, shown in Fig. 6.

However, if the galaxy had an inclination close to $i = 0°$, H II regions with a different position angle, i_e, could be observed through the slit. In this situation, we could observe regions with different radial velocity at the same apparent position (regions 1 and 2 in Fig. 5). For example, if we consider the mass density profile given in Section 4.1 (with $R_{DM} = 1$ kpc), we could measure changes in the radial velocity of 15 km s^{-1} between two regions with $x = 0$ and $x = 3$ kpc for $y = 2.5$ kpc (see Fig. 5). Therefore, the existence of inhomogeneities in the ionized gas distribution in the galaxy could also produce small-scale variations in its velocity field.

The emitting H II regions can, in principle, have any position angle $|i_e| \leq 180°$. In fact, a region with a given i_e at present, would evolve toward larger i_e angles in the future. Had all the H II regions been placed in planes of constant angle i_e, the resulting rotation curves would be the ones shown in Fig. 7.
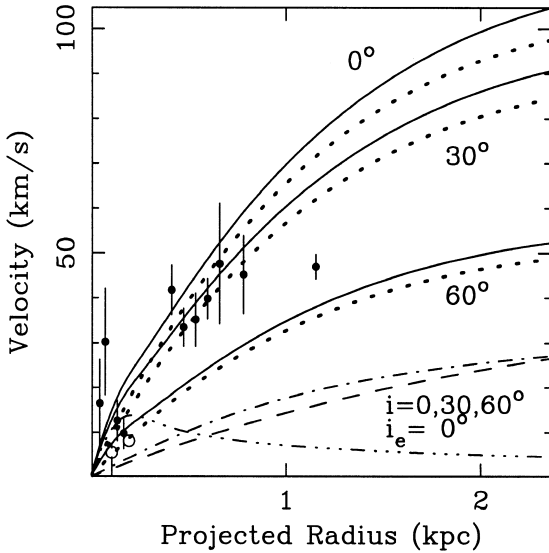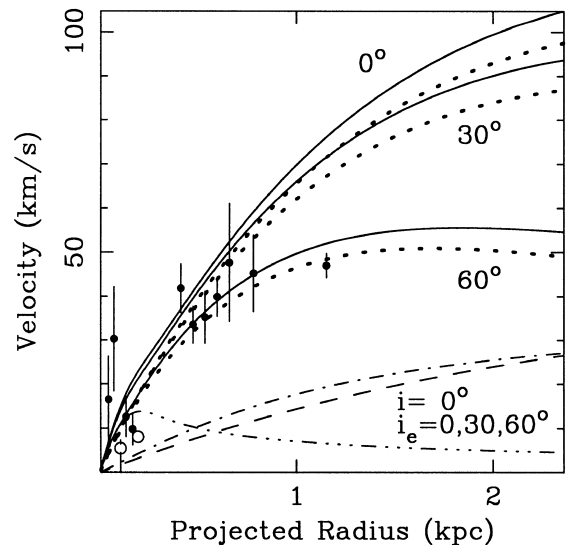

Figure 6. Total (solid) and stellar (dotted) radial velocity curve predicted for $i_e = 0°$ and inclination of the rotations axis, i, 0°, 30° and 60°. Black and white dots are, respectively, receding and approaching velocities. The dot-dot-dot-dashed, dot-dashed and dashed lines, the starburst, DM and HI density components represent respectively for only $i = 0°$ and $R_{DM} = 1$ kpc.

Figure 7. Radial velocity curves predicted for $i = 0°$ and $i_e = 0, 30, 60°$. The meaning of the symbols and line patterns are the same as in Fig. 6. Starburst, DM and HI density components are represented only for $i_e = 0°$ and $R_{DM} = 1$ kpc.

From Fig. 4 we see that the stellar mass density component dominates at the inner 4 kpc. However, the radial velocity data can be fitted by adopting different geometries for the ionized gas distribution (see Figs 6 and 7). We could reproduce the velocities measured if $i = 0°$ and $30° < i_e < 70°$, or if $i \simeq 40°$ and $i_e = 0°$.

On the other hand, the way the velocity gradient perpendicular to the rotation axis, ω, decreases from the equator to the galactic
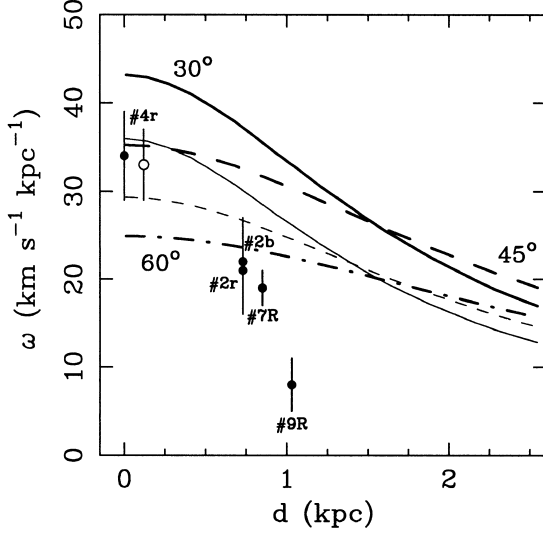

Figure 8. Change in the radial velocity gradients with the distance along the rotation axis. Data points have been taken from Table 2. For $d = 0$ we have taken the velocity gradient measured from the interpolated 2D velocity map. Thick lines represent the velocity gradient predictions for 30° (solid), 45° (dashed) and 60° (dot-dashed) inclined rotation axis with the density profile given in Section 4.1. Thin lines are the predictions for $i = 30°$ (solid) and 45° (dashed), but using $R_{under} = 0.5$ kpc, instead of 1.0 kpc. The open circle was obtained for a projected distance of -0.12 kpc east of the galactic centre (see Fig. 1).

outer regions (see Table 2) resembles the velocity fields observed in spiral galaxies with intermediate inclination (e.g. Giovanelli & Haynes 1988). We will test this point assuming that the emission observed effectively comes from a rotating thin disc with a gravitational potential similar to that given by the mass distribution described above (Section 4.1). Using this gravitational potential, we have estimated the expected radial velocity gradients for different distances, d, along the rotation axis (see Table 2). In Fig. 8 we show the gradients expected, measured as the change in radial velocity of their inner 2 kpc. Data points have been taken from Table 2. The value obtained for slit #9R is very uncertain because of the small number of points used to fit its velocity gradient (see Fig. 3). The zero value represents the gradient along the galactic equator obtained from the interpolated 2D velocity map. From this figure we note that, although a decrease in the velocity gradient is effectively observed, we cannot reproduce the values measured. The more feasible explanation is that the ionized gas is probably distributed in a relatively thick disc. However, the use of a steeper mass density profile could also reproduce the velocity gradients measured (see Fig. 8).

Therefore, we conclude that the observed global velocity field of Mrk 86 can be reproduced if the stellar component dominates the total mass profile within its optical radius, and if the emitting ionized gas is distributed in a (probably) thick inclined disc. The inclination of the disc with regard to the plane of the sky will be about 50° ($i \simeq 40°$).

5 KINEMATICAL EVIDENCE FOR SUPERNOVA-DRIVEN WINDS

Several under-kiloparsec-scale kinematical structures are observed superimposed on the global velocity gradients previously described. These kinds of kinematical disturbances have been widely observed in dwarf galaxies (see Tomita et al. 1997; Petrosian et al. 1997). Different mechanisms could properly

Table 3. Physical parameters of bubbles dE/dt_{kin} values given in the upper panel are deduced applying the expressions of r_{bubble} and v_{exp} from Castor, McCray & Weaver (1975). Lower panel shows the parameters of the best-fitting evolutionary LH model and the predicted collisionally excited Hα luminosity. Optical–near-infrared colours in parenthesis (upper panel) are those given by the corresponding LH model. $E(B - V)_{continuum}$ is assumed to be $0.44 \times E(B - V)_{gas}$ (Calzetti 1997). $E(B - V)_{gas}$ values for Mrk 86–A bubble have been obtained by M98 and this work (in parenthesis). Following the Castor, McCray & Weaver (1975) bubble model, dynamical ages, t_{dyn}, have been estimated as $0.6 \times r_{bubble}/v_{exp}$ (see, e.g., M98).

		A (big)[a]		B (N/S lobes)		C	
RA(B1950)		$08^h09^m40\overset{s}{.}0$		$08^h09^m42\overset{s}{.}3$		$08^h09^m41\overset{s}{.}1$	
Dec(B1950)		$46°08'25\overset{''}{.}0$		$46°08'6\overset{''}{.}5$		$46°08'52\overset{''}{.}6$	
r_{bubble}	(pc)	944		558/190		110	
v_{exp}	(km s^{-1})	47		40/28		17	
t_{dyn}	(Myr)	12		6.5		4	
dE/dt_{kin}	(erg s^{-1})	1.2×10^{40}		$2.5/0.1 \times 10^{39}$		8×10^{36}	
$L_{H\alpha}$	(erg s^{-1})	7×10^{37}		$0.5/2.5 \times 10^{38}$		1.7×10^{39}	
$E(B - V)_{gas}$		0.30	(0.13)	0.16		0.73	
m_B (knot)		17.12		17.77		17.65	
$B - V$		0.22 ± 0.06	(0.27)	0.17 ± 0.08	(0.19)	0.13 ± 0.08	(0.12)
$V - r$		-0.04 ± 0.02	(−0.10)	-0.11 ± 0.04	(−0.17)	0.05 ± 0.04	(0.00)
$r - K$		2.34 ± 0.09	(2.29)	2.1 ± 0.2	(2.11)	1.73 ± 0.17	(1.75)
Burst age	(Myr)	14.2		11.5		7.7	
Burst strength		~0.01		~0.01		~0.01	
Burst metallicity	(Z$_\odot$)	~0.25		~0.10		~0.10	
dE/dt_{kin}	(erg s^{-1})	2.2×10^{39}		1.4×10^{39}		9×10^{38}	
$L_{H\alpha}$ collis.	(erg s^{-1})	9×10^{36}		$2.4/1.7 \times 10^{36}$		2.3×10^{35}	
Mass	(M$_\odot$)	11×10^4		6×10^4		5×10^4	

[a] M98, converted to $H_0 = 50$ km s^{-1} Mpc^{-1}

explain these disturbances, including infalling motions of H II regions (Saitō et al. 1992) or inhomogeneities in the ionized gas distribution (see Section. 4). However, in our case, the deep minima (see Figs 3b,e,f and 12a and b below) and velocity maximum (Fig. 3e) observed are clearly spatially correlated with intense star-forming knots, indicating the existence of supernova-driven winds (see Sections 5.2, 5.3 and 5.4).

5.1   Description of the evolutionary synthesis models

In order to determine the physical properties of the star-forming knots, in particular, those associated with supernova-driven wind phenomena, we have made use of the Leitherer & Heckman (1995, hereafter LH) models. These single burst models do not take into account any contribution from the old underlying population or from emission lines (i.e. [O III]5007 Å, Hα).

Optical and near-infrared colours measured in the outer galaxy regions ($B - V = 0.8$, $V - r = 0.0$, $V - K = 2.5$; G98), where the exponential underlying population dominates (P96a), allow us to estimate an age of about 7 Gyr (G98 using the Bruzual & Charlot models) for this underlying component. Assuming different burst-strength values, ranging from 0.001 (0.1 per cent in mass) to 1, we have rebuilt a complete set of LH instantaneous burst models of 0.25 and 0.1 $Z_\odot$ metallicities, Salpeter IMF (Salpeter 1955) with $m = -2.35$, $M_{low} = 1\,M_\odot$ and $M_{up} = 100\,M_\odot$. Then, the relation (Kent 1985)

$$r = R + 0.41 + 0.21 \times (V - R) \qquad (6)$$

has been applied in order to transform from Johnson R to Gunn r magnitudes. Finally, using the Hα equivalent widths measured from the spectra, we have corrected the Gunn r magnitudes from Hα emission.

5.2   Previously detected Mrk 86–A bubble

Using long-slit echelle spectra in Hα+[N II] with 11 km s^{-1} resolution (FWHM), M98 inferred the presence of an expanding bubble extending 22 arcsec (940 pc) westward of the west end of
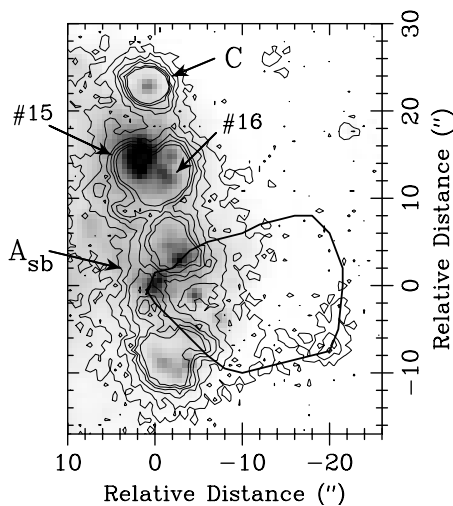

Figure 9. Mrk 86–A region. *B* image and Hα contours are shown. Displacements between *B*-band knots and Hα maxima are evident in the position of the Mrk 86–A bubble starburst precursor (M98), A$_{sb}$. The limits of the Mrk 86–A Hα emission given by M98 are also shown, joint with the positions of the #15 and #16 (G99) emission knots.

the galaxy. The physical parameters of this bubble are given in Table 3. In Fig. 9 we show the A (big bubble) region in Hα and *B*-band. Following M98, we have taken the knot marked in Fig. 9 as A$_{sb}$ (#31 emission knot in G99) as the starburst precursor.

For this region and for the Mrk 86–B and –C bubble precursors, we have determined physical apertures using the program COBRA (G99). This program determines and subtracts the underlying emission. The apertures include those pixels with emission more intense than 1/e times the emission maximum. Optical–near-infrared colours have been obtained for these apertures and corrected for internal extinction applying the relation given by Calzetti (1997), $E(B - V)_{continuum} = 0.44 \times E(B - V)_{gas}$. Using the H$\alpha$–H$\beta$ Balmer decrements and assuming a Mathis (1990) extinction law, colour excesses $E(B - V)_{gas}$ have been obtained. The corrected colours are given in Table 3. These colours allow us to estimate the mean physical properties – i.e. age, metallicity and burst strength – for these regions. In Table 3 we show the physical parameters of the LH model that better fits the colours measured.

In the Mrk 86–A case, the colours measured yield a LH model with 0.25-$Z_\odot$ metallicity, burst strength of 1 per cent and age of about 14 Myr (see Table 3). This value is slightly different from the dynamical time deduced by M98 (converted to $H_0 = 50$ km s^{-1} Mpc^{-1}), that is $t_{dyn} \simeq 12$ Myr. This discrepancy could be explained by taking into account that t_{dyn} describes the age of the expanding bubble, which differs from the starburst age by a period similar to the main sequence phase duration of the more massive stars. After the red supergiant phase has started ($\sim 4 \times 10^6$ yr after the starburst for $M \simeq 40\,M_\odot$; Maeder 1990), massive star winds and later supernova explosions would take place and a cavity of shock-heated gas could begin to form.

5.3   Mrk 86–B

A local velocity maximum and minimum are observed along the #4b slit velocity profile (see Fig. 3e). They differ by 68 km s^{-1} in velocity and are 10 arcsec (430 pc) apart. These features are compatible with the approaching (north lobe) and receding parts (south lobe) of a bipolar expanding structure with a characteristic projected expansion velocity of 34 km s^{-1}. The approaching velocity minimum is also observed in the #4r slit velocity profile (see Fig. 3f). Associated with these kinematical features is a clear bubble-like structure, observed in the Hα narrow-band image (see Fig. 10). Assuming a distance of 8.9 Mpc, a physical size of 750×510 pc^2 is obtained. This structure resembles those observed in I Zw 18 (Martin 1996), M82 (Heckman, Armus & Miley 1990) and NGC 1705 (MHW). The difference in size between both lobes could be related to a strong ambient density gradient, with higher density toward the south lobe region.

At 3 arcsec (130 pc) to the north-east from the geometrical centre of the bubble (origin of coordinates in Fig. 10) an optical emission knot (#49 in G99) is observed in the *B*, *V*, *r* and *K* bands (Fig. 10, left panel). If we compare the instantaneous burst evolutionary synthesis LH models to the colours measured (see Section 5.1 and Table 3), considering an age for the old underlying population of 7 Gyr (G98), the best fit obtained yields a starburst age of about 11.5 Myr, a burst strength of 1 per cent and a metallicity of about 0.1 $Z_\odot$. We are confident with the instantaneous burst assumption because we are dealing with single star-forming regions (LH). From the *B*-band total luminosity, and
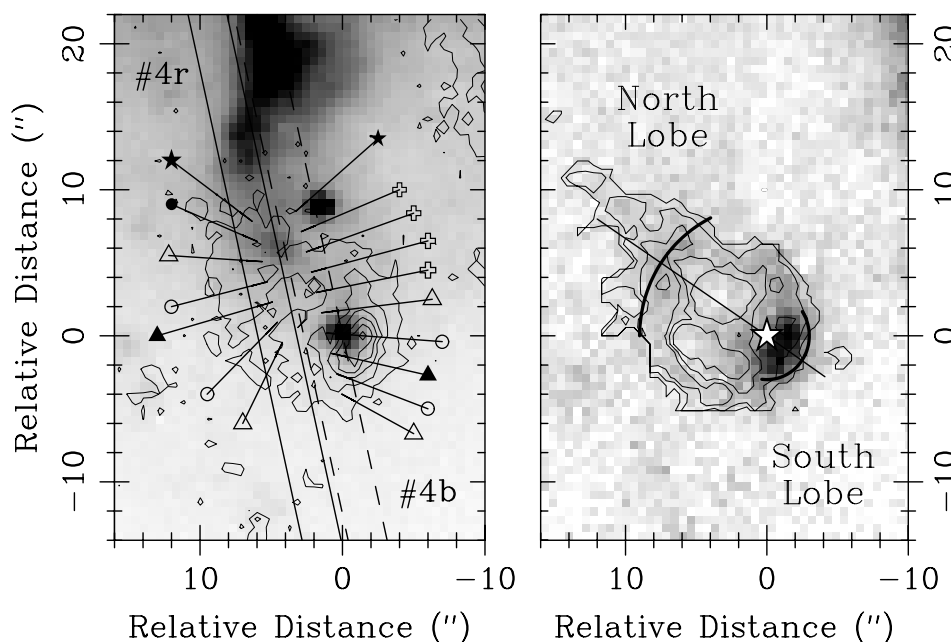
Figure 10. Left panel: Mrk 86–B region in *B*-band (image) and Hα (contours). Region 1 arcsec east and 9 arcsec north is a field star. Right panel: Hα (image) and [O III]/Hα (contours). See Figs 3(e) and (f) for the velocities measured in the regions marked on the left panel. In the [O III]/Hα case, some contour-map highly noisy regions have been artificially removed.

taking into account the burst strength derived, we estimate the involved total burst mass to be about $6.3 \times 10^4 \, M_\odot$.

Assuming that the kinematical features observed represent the foreground and receding parts of the expanding bubble, the dynamical age for this bubble, obtained as $t_{\text{dyn}} = 0.6 \times (r_S + r_N)/(v_S + v_N)$, will be about 6.5 Myr, quite similar to the evolution time deduced for the starburst region, if we consider the main-sequence time of massive stars, i.e. about 4–5 Myr, subtracting it from the starburst age (11.5 Myr).

Generally, it is accepted that the Hα luminosity observed in expanding bubbles is produced by photoionization from massive stars of the starburst precursor (MHW; Lehnert & Heckman 1996; Martin 1997). Then, the predicted collisionally excited Hα contribution should be irrelevant to the total Hα emission in the expanding lobes. The Hα luminosities measured for both lobes are $L_{\text{Hα}}^{\text{North}} = 4.7 \times 10^{37} \, \text{erg s}^{-1}$ and $L_{\text{Hα}}^{\text{South}} = 2.5 \times 10^{38} \, \text{erg s}^{-1}$. Considering that both lobes are well-reproduced by ellipsoids of revolution, we can obtain the lobe surface areas, that allow us to estimate the collisionally produced Hα luminosity

$$L_{\text{Hα}} \simeq S_{\text{lobe}} n_0 v_{\text{exp}} f h \nu_{\text{Hα}}, \tag{7}$$

where n_0 is the H I ambient density, v_{exp} the bubble expansion velocity, f is the number of Hα photons produced per shocked proton, and $\nu_{\text{Hα}}$ is the frequency of the Hα photons. The predicted collisionally excited luminosities are $L_{\text{Hα}}^{\text{North}} = 2.4 \times 10^{36} \, \text{erg s}^{-1}$ and $L_{\text{Hα}}^{\text{South}} = 1.6 \times 10^{36} \, \text{erg s}^{-1}$, less than 10 and 1 per cent (respectively) of the total Hα luminosity. We have assumed that approximately 0.1 Hα photons are produced per shocked proton. This is the value predicted by the Shull & McKee (1979) models for a 50 km s^{-1} shock. We have also adopted a H I ambient density of $n_0 \simeq 0.3 \, \text{cm}^{-3}$, that is the same value adopted by MHW for a sample of dwarf amorphous galaxies. This value is obtained by considering the Galactocentric distance of the Mrk 86–B

bubble, 1.2 kpc, and the Galaxy H I density profile given by equation (3).

As a result of the uncertainties present in the H I total mass and scale measurements, we could be dealing with significantly higher H I ambient densities (e.g. $n_0 \sim 1 \, \text{cm}^{-3}$), that could enhance the predicted collisional Hα luminosity. In any case, this contribution would not dominate the total Hα luminosity in the north lobe (< 30 per cent), and would be negligible in the south lobe case (~ 3 per cent).

Then, if the emission is photoionization dominated, the ratio between the luminosity of both lobes has to be related to the solid angle subtended from the starburst by each lobe. In fact, assuming revolution symmetry for both lobes, the solid angle ratio obtained is $\Omega_{\text{South}}/\Omega_{\text{North}} = 5.5$ ($\Omega_{\text{South}} = 6.6 \, \text{sr}$ and $\Omega_{\text{North}} = 1.2 \, \text{sr}$), very close to the ratio $L_{\text{Hα}}^{\text{South}}/L_{\text{Hα}}^{\text{North}} = 5.3$. In the right panel of Fig. 10 we show the aperture angles assumed, and the position of the ionizing radiation source (#49 knot in G99).

In order to estimate the relevance of the shock excitation mechanism, we have also studied the [O II]3727 Å/[O III]5007 Å, [O III]5007 Å/Hβ, [N II]6583 Å/Hα and ([S II]6717+6731 Å)/Hα line ratios across both lobes (see Figs 11a,b). For the south lobe region we obtain low excitation, log ([O III]/Hβ) $\simeq 0.3$, but with moderate log ([O II]/[O III]) $\simeq 0.3$ values. These values can be explained using photoionization models with a low ionization parameter (log U ~ -4; Martin 1997). However, for the more remote north lobe regions, the very high log ([O II]/[O III]) $\simeq 0.6$ (Fig. 11a) and high log ([N II]/Hα) $\simeq -0.5$ and log ([S II]/Hα) $\simeq 0$ (Fig. 11b) values obtained imply that an *additional* excitation mechanism should be present (Lehnert & Heckman 1996; Martin 1997). These line ratios are well reproduced by taking into account the emission predicted from the models of Shull & McKee (1979) with shock velocities of 90 km s^{-1}. This result is consistent with the higher collisional Hα luminosity predicted for the north lobe of the bubble.
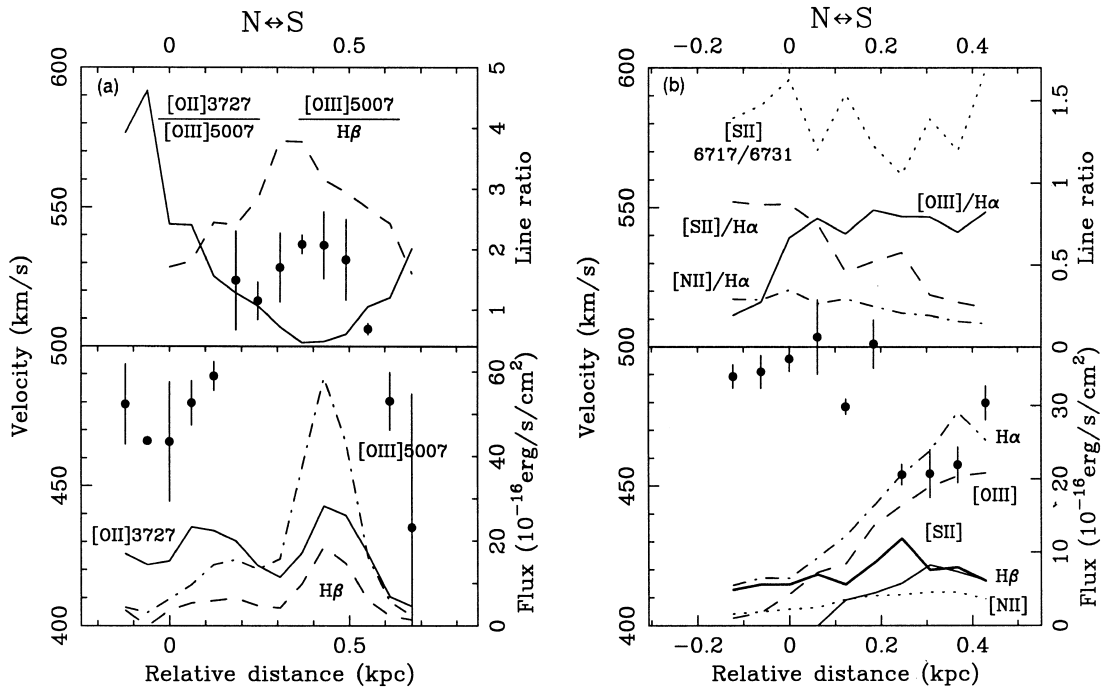
Figure 11. Mrk 86–B region. (a) Filled dots: #4b long-slit velocity profile. Upper panel: Observed [O II]/[O III] profile (solid line), [O III]/Hβ profile (dashed line). Lower panel: [O II] (solid), Hβ (dashed) and [O III] (dot-dashed) profiles. (b) Filled dots: #4r long-slit velocity profile. Upper panel: Observed [O III]/ Hα profile (solid), [S II]/Hα profile (dashed), [N II]/Hα profile (dot-dashed) [S II]6717 Å/[S II]6731 Å profile (dotted). Lower panel: Hβ (solid), [O III] (dashed), Hα (dot-dashed), [N II] (dotted), [S II] (thick solid). Relative distances refer to the same regions as in Figs 3(e) and (f).
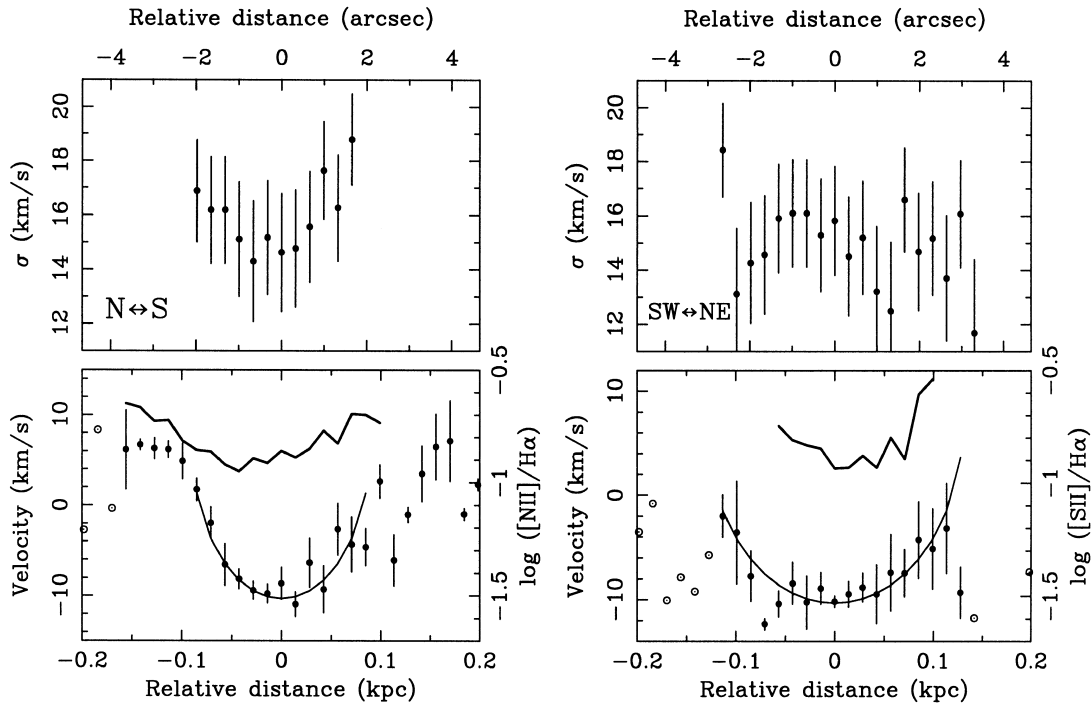
Figure 12. Mrk 86–C region. (a) #7R and (b) #8R long-slit velocity profiles. Upper panel: Velocity dispersion corrected from $\sigma_{instrumental}$. Lower panel: Filled circles represent the velocity data subtracted from large-scale velocity gradients. Dotted circles correspond to those velocities measured using just one emission line. $\pm 1\sigma$ errors bars have been plotted. Thin solid line represents the fit to an isotropic expanding bubble with $v_{exp} = 17.3 \, \text{km s}^{-1}$ and radii 90 and 130 pc, respectively. Thick lines show the [N II]/Hα (a) and [S II]/Hα (b) line ratio profiles relative to the bubble geometrical centre.

5.4 Mrk 86–C

From the high-resolution spectra #7R and #8R we infer the presence of deep velocity minima close to the G99 #9 knot emission maximum (C region in Figs 1 and 9). These minima, observed in both spectra #7R and #8R (see Figs 12a,b), are well understood if we are dealing with the foreground part of a largely extinct expanding bubble, with median parameters, $r_{\text{bubble}} = 110$ pc and $v_{\text{exp}} = 17.3$ km s^{-1} ($t_{\text{dyn}} \simeq 4$ Myr). These parameters (see Table 3) are obtained by fitting the radial velocity profiles (global velocity gradient subtracted; v_x) to an isotropic expanding structure velocity law (see Figs 12a,b),

$$v_x = v_{\text{exp}} \sqrt{1 - \frac{x^2}{r^2_{\text{bubble}}}}. \tag{8}$$

The central starburst should have a high extinction, large enough to obscure the Hα emission of the receding part of the bubble. In order to test this hypothesis we should estimate the physical properties, extinction included, of the starburst which has originated this collective wind.

The Mrk 86–C bubble has a similar appearance in all the optical and near-infrared images, including the Hα image (see Fig. 9), in contrast with the B bubble case, probably because of its lower dynamical time. Its Hα emission is slightly more extended along the west–east axis than that observed in broad-band filters. The corresponding optical and near-infrared colours measured for the starburst are given in Table 3 and are fully compatible with a 7.7-Myr-old and $Z = 0.1 Z_{\odot}$ metallic region, adopting, in order to better fit the colours measured, a colour excess of $E(B - V)_{\text{gas}} = 0.73$.

From these parameters, and the total B absolute magnitude measured, applying the LH results we obtain a starburst mass of about 4.7×10^4 M$_{\odot}$. In addition, because the total Hα luminosity measured for Mrk 86–C, 1.7×10^{39} erg s^{-1}, is 6×10^3 times higher than that predicted for the collisional case, 2.7×10^{35} erg s^{-1}, we can conclude that the line emission in Mrk 86–C is also mainly a result of photoionized gas.

Finally, we have studied the [N II]/Hα and [S II]/Hα line ratios measured from the high-resolution spectra. They change between ∼0.10 in regions close to the starburst centre, and ∼0.25 and ∼0.30, respectively, in the external low Hα surface brightness bubble regions (see Figs 12a,b). The increase in line ratio values towards bubble outer regions seems again to indicate a decrease in the ionization parameter because of the dilution of the radiation from the centralized source (Martin 1997). The values obtained are compatible with a pure low-metallicity H II region photo-ionization mechanism (see, e.g., Shields & Filippenko 1990).

6   VELOCITY DISPERSION IN MRK 86–C

We have measured the ionized gas velocity dispersion for the #7R and #8R high-resolution spectra. From the calibration lamp and night sky lines, we have estimated the spectral resolution in $\sigma_{\text{instrumental}} = 16.4 \pm 2.1$ km s^{-1}. Then, we have obtained the velocity dispersion of the Mrk 86–C bubble from these spectra, subtracting from $\sigma^2_{\text{observed}}$ the value of $\sigma^2_{\text{instrumental}}$. The spatial variation of the measured velocity dispersion is shown in Fig. 12. The velocity dispersion obtained for the *whole* (4.6×1 arcsec^2) bubble C were $\sigma_{7R} = 16 \pm 2$ km s^{-1} and $\sigma_{8R} = 15 \pm 2$ km s^{-1}. In addition, we have obtained the mean velocity dispersion for the

whole emitting region, averaging the values measured in intervals of 0.33, 1 and 2 arcsec along the spatial direction. We have estimated 17 ± 3 and 14.9 ± 1.6 km s^{-1}, respectively, for the #7R and #8R spectra and 0.33 arcsec intervals; 18 ± 5 and 15.4 ± 0.5 km s^{-1} for 1 arcsec intervals; and finally, 19 ± 5 and 15.2 ± 0.3 km s^{-1} for 2 arcsec intervals.

We observe that there is no significant difference between local and total velocity dispersion values, i.e. the velocity widths obtained for regions of size 0.33×1 arcsec^2 are similar to those obtained for an important fraction of the whole emitting region (4.6×1 arcsec^2), and that they do not change with the considered spatial interval.

We have now considered the expresion for the mass of a virialized system given by Guzmán et al. (1996, 1997; see also Bender, Burstein & Faber 1992 and Gallego et al. 1998),

$$M_{\text{vir}} = 1.184 \; 10^6 \, R_e \, (\text{kpc}) \, \sigma^2 \, (\text{km s}^{-1})^2 \, \text{M}_{\odot}. \tag{9}$$

If we take for Mrk 86–C the B-band effective radius of the starburst measured with COBRA, $R_e \simeq 36$ pc, and $\sigma \simeq 15$ km s^{-1}, we obtain a virialized mass (equation 9) for Mrk 86–C of about $M \sim 10^7$ M$_{\odot}$.

Let us compare this result with the Mrk 86–C starburst total mass estimated from the mass in newly formed stars ($M^{\text{young}}_{\text{burst}} = 5.3 \times 10^4$ M$_{\odot}$), underlying stellar population, gas and dark matter present in this region. Considering the mass density profile given in Section 4 we can estimate the mass content inside the effective radius of the Mrk 86–C starburst precursor. Assuming the most favourable case, i.e. $i_e = 0°$ and a dark matter model with $R_{\text{DM}} = 2^{1/2} \times r$, the density expected at a galactocentric distance of 1.0 kpc, will be 9 atom$_H$ cm^{-3}. Therefore, the mass content inside R_e should be about 10^5 M$_{\odot}$. We can conclude that the burst total mass is significantly lower than the virialized mass deduced. The similarity of the velocity dispersion measured pixel by pixel rules out the global velocity gradient as the origin for the observed velocity dispersion. The first reason for Mrk 86–C not to be bound arises from the existence of local gas motions induced by the Mrk 86–C supernova-driven wind. Another argument is that Mrk 86–C is not placed at the galactic centre and, therefore, is subject to strong tidal forces that prevent it from being virialized.

We have obtained the turbulent velocity dispersion[2] (see, e.g., Fuentes-Masip 1997), applying the expression

$$\sigma^2_{\text{turbulent}} = \sigma^2_{\text{observed}} - \sigma^2_{\text{thermic}} - \sigma^2_{\text{intrinsic}} - \sigma^2_{\text{instrumental}}, \tag{10}$$

which yields $\sigma_{\text{turbulent}} \simeq 10.7$ km s^{-1} and 10.0 km s^{-1}, respectively, for #7R and #8R spectra, assuming for Hα a $\sigma_{\text{intrinsic}} = 7.1$ km s^{-1} (Hippelein 1986), and a temperature $T = 10^4$ K. Adopting a sound velocity for the ionized gas in H II regions of about 12.8 km s^{-1} (Dyson & Williams 1980), the corresponding σ_{sound} is approximately 8 km s^{-1} (Fuentes-Masip 1997). Thus, we can conclude that the velocity dispersion in this region is sonic or slightly supersonic.

7   SUMMARY AND CONCLUSIONS

(i) The global velocity field in Mrk 86 has a central angular velocity of about 34 km s^{-1} kpc^{-1} with orientation PA ∼ 12° (rotation axis PA ∼ −78°). This velocity gradient shows a

---

[2] Turbulent velocity dispersion is defined as the line broadening obtained after subtracting instrumental and thermal broadening.

progressive diminution towards outer galaxy regions, from $34\,\mathrm{km\,s^{-1}\,kpc^{-1}}$ at the Galactic Centre to $\sim 10\,\mathrm{km\,s^{-1}\,kpc^{-1}}$ at 1 kpc. The density profiles of the different mass components indicate that the underlying stellar component dominates the total mass within its optical radius. The velocity gradients measured for different distances along the Galactic rotation axis indicate that the ionized gas is probably distributed in an inclined rotating disc, with inclination in relation to the plane of the sky of about $50°$.

(ii) High-velocity gradients of about $70\,\mathrm{km\,s^{-1}\,kpc^{-1}}$ associated with intense star-forming regions have been observed. Either a high-mass concentration or a recent merger could be responsible for these local, steep velocity gradients.

(iii) Our observations have revealed the existence of two bubbles, Mrk 86–B and Mrk 86–C. They present v_{exp} of 34 and $17\,\mathrm{km\,s^{-1}}$ and r_{bubble} of 374 and 120 pc, respectively. These structures are driven by supernovae and massive star winds that originated in two low-metallicity ($Z \sim 0.1\,Z_\odot$) H II regions 11 and 8 Myr old, with masses of 6.3×10^4 and $5.3 \times 10^4\,\mathrm{M_\odot}$. The H$\alpha$ emission is dominated by photoionization mechanisms, contributing at least 90 per cent of the total Hα luminosity. Moreover, the measured optical line ratios agree with photoionization mechanisms as the origin for their emission.

(iv) In addition, we have studied the physical properties of the starburst precursor of the Mrk 86–A bubble described by Martin (1998). The optical–near-infrared colours measured for these regions are well described by a 14-Myr-old, low-metallicity ($Z \sim 0.25\,Z_\odot$), $10^5\,\mathrm{M_\odot}$ massive starburst.

The predicted starburst ages agree quite well with the dynamical times measured if we assume a delay of ~ 4 Myr between the starburst formation and the time when the bubble begins to inflate. In fact, the one-tenth solar metallicity Leitherer & Heckman (1995) models predict an increment of about 1.5 dex in the deposition rate of mechanical energy 4 Myr after the star formation burst.

(v) The global velocity dispersion obtained for Mrk 86–C does not trace the total mass of the burst. The turbulent velocity dispersion obtained for the Mrk 86–C bubble is sonic or slightly supersonic, with $\sigma_{\mathrm{turbulent}} \sim 10\,\mathrm{km\,s^{-1}}$. These values do not show significant changes across the region.

REFERENCES

Aragón-Salamanca A., Ellis R. S., Couch W. J., Carter D., 1993, MNRAS, 262, 764

Arp H., 1966, Atlas of Peculiar Galaxies. California Institute of Technology, Pasadena

Bender R., Burstein D., Faber S. M., 1992, ApJ, 399, 462

Binney J., Tremain S., 1987, in Ostriker J. P., ed., Galactic Dynamics. Princeton Univ. Press, Princeton NJ

Bomans D. J., Chu Y. H., Hopp U., 1997, AJ, 113, 1678

Bottinelli L., Gouguenheim L., Paturel G., de Vaucouleurs G., 1984, A&AS, 56, 381

Brinks E., 1994, in Tenorio-Tagle G., ed., Violent Star Formation: From 30 Doradus to QSOs. First IAC-RGO meeting, La Palma, Cambridge University Press, New York, p. 145

Broeils A. H., 1992, PhD thesis, Rijksuniversiteit Groningen

Burkert A., 1995, ApJ, 447, 25

Calzetti D., 1997, in Waller W. H., ed., AIP Conf. Proc., Vol. 408, The Ultraviolet Universe at Low and High Redshift: Probing the Progress of Galaxy Evolution. American Institute of Physics, New York, p. 403

Carignan C., Beaulieu S., 1989, ApJ, 347, 760

Carignan C., Freeman K. C., 1988, ApJ, 332, L33

Castor J., McCray R., Weaver R., 1975, ApJ, 200, L107

Chevalier R., Clegg A., 1985, Nat, 317, 44

De Vaucouleurs G., Pence W. D., 1980, ApJ, 242, 18

De Young D. S., Gallagher J. S., 1990, ApJ, 356, L15

Dultzin-Hacyan D., Masegosa J., Moles M., 1990, A&A, 238, 28

Dyson J. E., Williams D. A., 1980, The Physics of the Interstellar Medium. Manchester University Press, Manchester

Fanelli M. N., O'Conell R. W., Thuan T. X., 1988, ApJ, 334, 665

Flores R. A., Primack J. R., 1994, ApJ, 427, L1

Fuentes-Masip O., 1997, PhD thesis, Universidad de La Laguna

Gallego J., Zamorano J., García-Dabó C. E., Aragón-Salamanca A., Guzmán R., 1998, in D'Odorico S., Fontana A., Giallango E., eds., ASP Conf. Ser. Vol. 146, The Young Universe, Astron. Soc. Pac., San Francisco, p. 235

Gil de Paz A., Zamorano J., Gallego J., 1998, in Thuan T. X., Balkowski C., Cayatte V., Tran Tranh Van J., eds, 118th Moriond Meeting, Dwarf Galaxies and Cosmology. Editions Frontières, Gif-sur-Yvette (G98)

Giovanelli R., Haynes M. P., 1988, in Verschuur G. L., ed., Galactic and Extragalactic Radio Astronomy. Springer-Verlag, New York, p. 522

Guzmán R., Koo, D. C., Faber S. M., Illingworth G. D., Takamiya M., Kron R. G., Bershady M. A., 1996, ApJ, 460, L5

Guzmán R., Gallego J., Koo D. C., Phillips A. C., Lowenthal J. D., Faber S. M., Illingworth G. D., Vogt N. P., 1997, ApJ, 489, 559

Heckman T. M., Armus L., Miley G. K., 1990, ApJS, 74, 833

Hippelein H., 1986, A&A, 160, 374

Hodge P., Kennicutt R. C., 1983, AJ, 88, 296

Israel F. P., Tacconi L. J., Baas F., 1995, A&A, 295, 599

Izotov Y. I., Dyak A. B., Chaffee F. H., Foltz C. B., Kniazev A. Y., Lipovetsky V. A., 1996, ApJ, 458, 524

Kamphuis J. J., Sijbring L. G., van Albada T. S., 1996, A&AS, 116, 15

Kent S. M., 1985, PASP, 97, 165

Klein U., Wielebinski R., Thuan T. X., 1984, A&A, 141, 241

Klein U., Weiland H., Brinks E., 1991, A&A, 246, 323

Lehnert M. D., Heckman T. M., 1996, ApJ, 462, 651

Leitherer C., Heckman T. M., 1995, ApJS, 96, 9 (LH)

Lo K. Y., Sargent W. L. W., Young K., 1993, AJ, 106, 507

Longo G., Capaccioli M., Ceriello A., 1991, A&AS, 90, 375

Lonsdale C. J., Helou G., Good J. C., Rice W., 1985, Catalogued Galaxies and Quasars Observed in the IRAS Survey. Jet Propulsion Lab, Pasadena CA

Loose H.-H., Thuan T. X., 1985, in Kunth D., Thuan T. X., Van J. T. T., eds, Star-Forming Dwarf Galaxies. Editions Frontières, Gif-sur-Yvette

Loose H. H., Thuan T. X., 1986, ApJ, 309, 59

MacLow M.-M., Ferrara A., 1999, ApJ, 513, 142

Maeder A., 1990, A&AS, 84, 139

Markarian B. E., 1969, Afz, 5, 443

Marlowe A., Heckman T. M., Wyse R. F. G., Schommer R., 1995, ApJ, 438, 563 (MHW)

Martin C. L., 1996, ApJ, 465, 680

Martin C. L., 1997, ApJ, 491, 561

Martin C. L., 1998, ApJ, 506, 222 (M98)

Mathis J. S., 1990, ARA&A, 28, 37

Meurer G. R., StaveleySmith L., Killeen N. E. B., 1998, MNRAS, 300, 705

Moore B., 1994, Nat, 370, 629

Mori M., Yuzuru Y., Takuji T., Ken'ichi N., 1997, ApJ, 478, L21

Navarro J. F., Eke V. R., Frenk C. S., 1996, MNRAS, 283, 72

Navarro J. F., Frenk C. S., White S. D. M., 1997, ApJ, 490, 493 (NFW)

Ojha D. K., Joshi S. C., 1991, Ap&SS, 183, 245

Östlin G., Amram P., Masegosa J., Bergvall N., Boulesteix J., 1999, A&AS, in press

Papaderos P., Loose H.-H., Thuan T. X., Fricke K. J., 1996a, A&AS, 120, 207 (P96a)

Papaderos P., Loose H.-H., Fricke K. J., Thuan T. X., 1996b, A&A, 314, 59 (P96b)

Petrosian A. R., Boulesteix J., Comte G., Kunth D., LeCoarer E., 1997, A&A, 318, 390

Puche D., Westphal D., Brinks E., Roy J. R., 1992, AJ, 103, 1841

Roy J. R., Boulesteix J., Joncas J., Grundseth B., 1991, ApJ, 367, 141

Sage L. J., Salzer J. J., Loose H. H., Henkel C., 1992, A&A, 265, 19

Saitō M., Sasaki M., Ohta K., Yamada T., 1992, PASJ, 44, 593

Salpeter E. E., 1955, ApJ, 121, 161

Salucci P., Persic M., 1997, in Persic M., Salucci P., eds, ASP Conf. Ser. Vol. 117, Dark and Visible Matter in Galaxies. Astron. Soc. Pac., San Francisco, p. 1

Scalo J. M., 1986, Fundam. Cosmic Phys., 11, 1

Shapley H., Ames A., 1932, Ann. Harvard College Obs., 88, No. 2

Shields G. A., Filippenko A. V., 1990, AJ, 100, 103

Shull S. M., McKee C., 1979, ApJ, 227, 131

Silk J., Wyse R. F. G., Shields G., 1987, ApJ, 322, L59

Skillman E. D., Kennicutt R. C., 1993, ApJ, 411, 655

Staveley-Smith L., Davies R. D., Kinman T. D., 1992, MNRAS, 258, 334

Swaters R., 1998, in Merritt D. R., Valluri M., Sellwood A., eds., ASP Conf. Ser., Galaxy Dynamics. Astron. Soc. Pac., San Francisco, to appear

Thuan T. X., 1983, ApJ, 268, 667

Thuan T. X., 1991, in Leitherer C., Walborn N. R., Heckman T. M., Norman C. A., eds, STScI Symp. Ser. 5, Massive Stars in Starburst. STScI, Baltimore, p. 183

Thuan T. X., Martin G. E., 1981, ApJ, 247, 823

Tomita A., Ohta K., Nakanishi K., Takeuchi T. T., Saitō M., 1997, AJ, 116, 131

Vader J. P., 1986, ApJ, 305, 669

Vader J. P., 1987, ApJ, 317, 128

van Zee L., Skillman E. D., Salzer J. J., 1998, AJ, 116, 1186

Verter F., 1985, ApJS, 57, 261

Young J. S., Knezek P., 1989, ApJ, 347, L55

This paper has been typeset from a TEX/LATEX file prepared by the author.